PAPER • **OPEN ACCESS**

Validation of an analytical approach for *in vivo* PET verification in carbon ion therapy: comparison with Monte Carlo simulations and PET monitoring measurements

To cite this article: Tianxue Du *et al* 2026 *Phys. Med. Biol.* **71** 095010

Physics in Medicine & Biology

IPEM Institute of Physics and Engineering in Medicine

OPEN ACCESS

RECEIVED
14 December 2025

REVISED
31 March 2026

ACCEPTED FOR PUBLICATION
20 April 2026

PUBLISHED
5 May 2026

PAPER

Validation of an analytical approach for *in vivo* PET verification in carbon ion therapy: comparison with Monte Carlo simulations and PET monitoring measurements

Tianxue Du[1,*], **Julia Bauer**[2,3,6], **Thomas Tessonnier**[2,4,5], **Katia Parodi**[1,7] and **Marco Pinto**[1,7]

[1] Ludwig-Maximilians-Universität München, Department of Medical Physics, Munich, Germany
[2] Department of Radiation Oncology, Heidelberg University Hospital, Heidelberg, Germany
[3] Heidelberg Institute of Radiation Oncology (HIRO), Heidelberg, Germany
[4] Heidelberg Ion-Beam Therapy Center (HIT), Heidelberg, Germany
[5] Clinical Cooperation Unit Radiation Oncology, National Center for Tumor Diseases (NCT), Heidelberg University Hospital (UKHD) and German Cancer Research Center (DKFZ), Heidelberg, Germany
[6] Now at Department of Radiation Oncology, Charité—Universitätsmedizin Berlin, Corporate Member of Freie Universität Berlin and Humboldt-Universität zu Berlin, Berlin, Germany.
[7] The two authors contributed equally to this work.
[*] Author to whom any correspondence should be addressed.

E-mail: t.du@physik.uni-muenchen.de

Keywords: carbon ion therapy, range verification, positron emission tomography, offline PET, analytical prediction

Abstract

Objective. As carbon ion therapy is highly sensitive to range uncertainties, it can benefit greatly from range verification. Positron emission tomography (PET) provides a valuable approach, in which predicted positron emitter distributions (PED) can be used to calculate the expected activity distribution, which is then compared with the irradiation-induced PET signal. In a previous work, we developed an analytical approach to predict 3D PED from dose distributions, providing a faster alternative to Monte Carlo (MC) simulations at a comparable accuracy, and with potential for integration into analytical treatment planning systems (TPS). The purpose of this work is to validate this analytical approach using real clinical cases where offline PET/Computed tomography (CT) monitoring was employed. *Approach*. Four carbon ion therapy patients treated at the Heidelberg Ion Beam Therapy Center were selected, and their treatment plans and CT images were used for MC simulations and analytical prediction of β^+-activity distributions. The analytically predicted activity distributions, derived from the simulated dose distributions with our analytical approach, were then compared with both simulated results and measured offline PET data. *Main results*. The analytical and MC activity distributions demonstrated a good match in range with mean deviations less than 0.5 mm, and in amplitude with mean normalized root-mean-square error less than 2%. Range shifts between the measured PET signals and the analytical activity patterns were evaluated and found to be consistent with published results. *Significance*. The obtained results demonstrate the capability of our analytical approach to predict PET images for range verification in carbon ion therapy under real clinical scenarios, offering faster predictions than MC simulations while maintaining comparable accuracy. The solution proposed also offers the possibility of a straightforward integration into TPS by leveraging the commonly used pencil beam algorithms present in analytical carbon ion dose engines.

1. Introduction

Carbon ion therapy has been increasingly applied worldwide as an effective treatment for cancer due to its unique dose distribution and relative biological effectiveness advantages compared to conventional photon radiotherapy (Malouff *et al* 2020). However, carbon ion therapy is sensitive to range uncertainties

because small deviations in beam range can significantly impact clinical outcomes by causing underdosage of the tumor or unnecessary radiation exposure to normal tissue. Therefore, range verification is desirable to achieve higher levels of treatment quality assurance. Positron emission tomography (PET) has been widely applied for treatment monitoring, as it detects positron-emitting isotopes generated through nuclear interactions between carbon ions and the medium, providing indirect, non-invasive range verification (Oelfke *et al* 1996, Parodi *et al* 2005, Combs *et al* 2012, Yoshida *et al* 2017, Moglioni *et al* 2022). Since the PET signal is not directly proportional to the delivered dose, because of their different underling nuclear and electromagnetic interactions, measured PET activity distributions need to be compared against predicted distributions derived either through Monte Carlo (MC) simulations (Pönisch *et al* 2004, Parodi *et al* 2007b, Bauer *et al* 2013, Frey *et al* 2014, Pennazio *et al* 2018) or analytical approaches (Priegnitz *et al* 2012, Helmbrecht *et al* 2016, Hofmann *et al* 2019, Du *et al* 2025). Although highly accurate, MC methods require significant computational effort and are time-consuming. Recent developments in GPU-accelerated fast MC tools have largely reduced the computation time, achieving high accuracy for dose calculation (Jia *et al* 2012, Schiavi *et al* 2017, Choi *et al* 2018, Lysakovski *et al* 2024) and PET-based range verification (Borys *et al* 2022, McNamara *et al* 2022). However, their application in carbon ion therapy, particularly for PET-based range verification, remains non-existent to the best of our knowledge.

Experimental-based approaches have predicted positron emitter distributions (PED) using linear superposition of measured yields from different reference materials (Priegnitz *et al* 2012). This approach was extended to 3D calculations but exhibited limitations in lateral beam description and projectile fragment prediction (Helmbrecht *et al* 2016). Another 1D analytical method adapted a filtering approach originally designed for proton therapy (Parodi and Bortfeld 2006) to carbon ions (Hofmann *et al* 2019). However, it was primarily validated in 1D or quasi-3D scenarios (Vasic *et al* 2024), and demonstrated suboptimal performance in cases with large heterogeneities, such as air cavities. Recently, a 3D analytical approach based on an improved version of the latter 1D approach and its integration into a pencil beam algorithm (PBA) framework was proposed and validated by in-silico studies which showed good agreements to MC simulations (Du *et al* 2025).

In this work, we aim to validate this analytical approach for in-vivo PET verification in carbon ion therapy under real clinical conditions, by comparing the analytical predictions against both MC simulations and offline PET measurements for four patient cases treated at the Heidelberg Ion Beam Therapy Center (HIT).

2. Material and methods

2.1. Subject selection

Four patients undergoing carbon ion therapy at HIT were selected for this study (Bauer *et al* 2013, Kurz *et al* 2016). The cohort included one patient with a brain tumor (BR), one with a head&neck tumor (HN), one with a liver tumor (LIV), and one with a pelvic tumor (PEL). Offline PET monitoring was employed for treatment verification. Each patient received pencil beam scanning irradiation in the treatment room, followed by PET/Computed tomography (CT) scanning in a separate room equipped with a commercial PET/CT scanner. More details on the patient workflow and data acquisition are described in Bauer *et al* (2013). The anonymized HIT clinical datasets used for this study include the treatment planning CT (TP-CT) images, treatment plans, PET images and FLUKA MC simulated dose-to-water distributions (dose-to-tissue distributions were not available). An overview of the patient cases is provided in table 1.

2.2. MC simulations

MC simulations were conducted using the Geant4 toolkit (Agostinelli *et al* 2003) version 10.07.p04 to obtain dose (both dose-to-tissue and dose-to-water) and PED spot by spot based on patient-specific treatment plans and CT-derived geometry. The simulated dose-to-tissue distributions were used as the input for the following analytical prediction, whereas the dose-to-water distributions were used for comparison with the FLUKA MC results from HIT. The physics list QGSP_BIC (quark-gluon string precompound, binary light ion cascade package) was selected for the modeling of physical processes, based on the findings of Chacon *et al* (2019, 2024), who concluded that the BIC model of Geant4 provided the best overall agreement of predicted positron-emitting fragment yields in comparison to experimental ^{12}C ion beam measurements. In total five positron emitters (PEs), ^{11}C, ^{10}C, ^{15}O, ^{13}N and ^{14}O, were considered and scored to keep consistency with PEs predicted by the analytical approach. The rationale for selecting these isotopes is detailed in section 2.3.

Table 1. Details of the clinical datasets used in this study: one brain tumor BR, one head/neck tumor HN, one liver tumor, LIV and the pelvic tumor PEL. Treatments details include energy range, number of ions to be delivered according to the plan ('IonsTP'), the irradiation time (t_{irr}), the time between end of irradiation and PET imaging (Δt), the PET-imaging duration (t_{PET}).

Patient ID	Energy (MeV/n)	IonsTP	t_{irr} (min:s)	Δt (min:s)	t_{PET} (min:s)
BR	89-208	0.53E09	03:58	08:15	30:00
HN	98-210	1.02E09	06:10	05:29	30:00
LIV	209-315	8.77E09	29:03	12:03	30:00
PEL	219-430	8.40E09	14:28	09:26	30:00

Note: The long treatment time for the LIV case was due to respiratory gating. The PEL patient received two separate treatment plans delivered on alternating days to ensure full target coverage. Only one of these plans is presented in this study, and this single-field plan naturally exhibits limited dose coverage, which is reflected in the corresponding dose images.

For the purpose of comparing our results with HIT's measurement data, we must ensure that our simulation settings accurately replicate HIT's scanned ion beam delivery. Fortunately, the relevant FLUKA MC modeling had already been implemented for producing the input of the analytical planning system (Parodi *et al* 2012) and the full MC framework was used in routine clinical workflows (Bauer *et al* 2014). To allow meaningful comparisons with experimental data, consistency between our MC and HIT MC simulations was guaranteed by replicating the clinical beam configuration and matching the CT-range calibrations across different CT acquisition protocols. Specifically, the clinical beam configuration was reproduced using input phase space data (Tessonnier *et al* 2016), which were produced with the FLUKA MC code incorporating the detailed beamline model described in Parodi *et al* (2013). The CT-to-material conversion method followed the stoichiometric calibration of Schneider *et al* (2000), Parodi *et al* (2007a). We applied an additional correction to the internal Geant4 stopping power ratio (SPR) calculation of CT-derived materials for consistency to the clinically used CT-SPR calibration curves (depending on anatomical site). The SPR is defined as the ratio of the stopping power of carbon ions in a material to that in water at a specific energy. These corrections were implemented by tuning the mean excitation potential (I) of CT-derived materials to match the CT-SPR tables used at HIT at the energy of 120 MeV/n. Finally, CT-I lookup tables were built and incorporated into our MC simulations. We validated the consistency by comparing our simulated dose-to-water of the four patient cases with the FLUKA MC results from HIT. It is important to note that the same FLUKA MC engine was also employed to generate the clinical TP systems (TPS) database (SyngoPT, Siemens and RayStation, RaySearch Lab) at HIT (Parodi *et al* 2012, Bauer *et al* 2014).

2.3. Analytical approach

Our dedicated analytical calculation framework, based on a PBA, predicts 3D PED from dose distributions (Du *et al* 2025). This framework follows a structure similar to the PBA proposed by Soukup *et al* (2005) for 3D dose computation, requiring the laterally integrated depth PED (IDPED), lateral properties parameterization, and patient and beam information, as detailed below. Both the IDPED and the lateral properties parameterization involve dedicated pre-calculation work based on MC simulations, which are also outlined below.

- **IDPED** is derived from the laterally integrated depth dose (IDD) at corresponding energies in a reference material using analytical functions combined with a filtering approach (see appendix for details). The reference material consists of six elements (H, C, N, O, P and Ca) that contribute to the main production of PEs in human tissue with its properties summarized in table 2. The parameters of these analytical functions were predefined using IDD and IDPED data from the MC simulations in the reference material for initial energy from 80 to 430 MeV/n in 10 MeV/n increments (see Du *et al* 2025 for simulation details). As reported in Du *et al* (2025), PEs generated from the fragmentation of phosphorus (^{30}P) and calcium (^{38}K) in the reference material were negligible and were therefore excluded from the analytical model. Ultimately, five isotopes ^{11}C, ^{10}C, ^{15}O, ^{13}N and ^{14}O, which are the most relevant PEs in carbon ion therapy (Pönisch *et al* 2004) were considered in the analytical approach. The analytical approach calculates IDPEDs for the five PEs. Specifically, it classifies them based on their kinetic characteristics into projectile and target fragmentation groups: five target PEs ($^{11}C_{target}$,

Table 2. The reference material properties.

Mass density ($g{\cdot}cm^{-3}$)	Electron density (10^{23} cm^{-3})	Mass abundances (%)					
		H	C	N	O	P	Ca
1.54	4.71	2	31	26	38	1	3

$^{10}C_{target}$, ^{15}O, ^{13}N, and ^{14}O) and two projectile PEs ($^{11}C_{proj}$ and $^{10}C_{proj}$), each modeled by distinct functions.

- **Lateral properties parameterization:** The same set of MC simulations employed for the precalculation of IDPED analytical functions were used here. The lateral properties of PED were predefined by fitting the MC-calculated PED in the reference material at different depths and representative initial energies between 80 and 430 MeV/n, using either a single Gaussian for the projectile fragments or a double Gaussian function for the target fragments.
- **Patient and Beam information:** The modeling of the patient anatomy deduced from the CT images includes mass density, electron density, mass fractions of constituent elements, and I of each voxel. Beam-related information includes the incident direction, position, energy, and spot size for each beam.

In practical applications, the analytical algorithm only requires the corresponding 3D dose-to-tissue distributions and the beam and patient information. The analytical prediction begins by reading the 3D dose-to-tissue distribution of a single spot. In this study, the dose distribution for each beam spot in the treatment plans was first calculated through MC simulations. This 3D dose distribution was converted to a 3D dose in the reference material by tracing each beam ray to obtain its depth–dose profile and converting it to the corresponding equivalent depth in the reference material. The resulting dose distribution was then laterally integrated to generate the reference IDD. Next, the IDPEDs of the five target PEs and two projectile PEs generated from different target nuclei in the reference material were then built based on the reference IDD we built before. We applied the same CT-to-material conversion method as that used in the MC simulations to build the material information of the patient anatomy, including the mass density, electron density, and mass abundances. The I value of material was got from the same CT-I lookup table employed in the MC simulations. Finally, using predefined parameterization of the lateral properties of PED, along with beam parameters including the initial beam size and energy, the algorithm spreads the IDPEDs into 3D PED, accounting for the phantom's heterogeneity (Du *et al* 2025).

In the context of this work, the dose-to-tissue distributions were calculated using MC simulations, which served as the required input of the analytical approach. However, when the analytical approach is deployed and commissioned in the clinical workflow, the dose-to-tissue per spot can be retrieved from the TPS without any need for MC simulations. If the TPS provides dose-to-water rather than dose-to-tissue, the same conversion procedure described above can be applied, except that only the dose values need to be rescaled from water to the reference material according to the corresponding mass SPR.

2.4. Activity calculation

To compute the activity pattern from the analytical or simulated PED, it is necessary to account for both the time course of measurement (cf table 1) and the biological washout PEs. The PEs are generated during the irradiation and may undergo radioactive decay during the treatment session, the subsequent patient transport, or the PET measurement. In addition to the physical decay, the activity distribution is affected through the biological washout which depends primarily on tissue perfusion. Following the model described in Mizuno *et al* (2003), Parodi *et al* (2007b), tissue is segmented according to CT Hounsfield units into regions of low, intermediate, or normal perfusion, though only the slow component of washout is considered here, given the relatively large time delays between irradiation and imaging (Δt). Each tissue region is assigned a distinct biological decay constant λ_{bio} and a relative fraction M_s of the slow-decay component, with parameter values also reported in Mizuno *et al* (2003), Parodi *et al* (2007b)and later used also in the HIT clinical PET study (Bauer *et al* 2013). Taking these factors into account, an expected activity pattern $\langle A(r)\rangle$ averaged over the PET imaging time t_{PET} can be calculated according to Parodi *et al* (2007b), Bauer *et al* (2013), neglecting the slow biological washout during the short irradiation time, as follows:

$$\langle A(r)\rangle = G(r)\cdot\sum_j\left[\, M_s(r)\,PED_j(r)\cdot\frac{\left[1-\exp\left(-\lambda_{phys,j}\cdot t_{irr}\right)\right]}{t_{irr}}\cdot\exp\left(-\lambda_{tot,j}(r)\cdot\Delta t\right)\cdot\frac{\left[1-\exp\left(-\lambda_{tot,j}(r)\cdot t_{PET}\right)\right]}{\lambda_{tot,j}(r)\cdot t_{PET}}\,\right] \quad (1)$$

where $G(r)$ is the three-dimensional Gaussian point spread function modeling the spatial resolution of the PET scanners, $PED_j(r)$ is the PED for the jth PE calculated by either the simulation or the analytical prediction, and λ_{tot} is the total decay constant given by the sum of λ_{bio} and the physical decay constant λ_{phys}.

2.5. Data analysis

We first compared our simulated dose-to-water of the four patient cases with MC results from HIT by global gamma analysis to verify consistency between our simulations and those from HIT. Next, we compared the analytically predicted PET results with both MC simulated results and measured data to verify the capability of our analytical approach for range verification in clinical scenarios. 1D activity profiles along the selected line in beam direction for each case were plotted to illustrate the magnitude and range of the analytical, simulated and measured activity. To assess the longitudinal shifts, we extracted 1D activity profiles along the beam direction for each (x,y) in the transverse plane from the two 3D distributions to be compared and employed a most-likely-shift (MLS) method, as detailed in the following sections. Additionally, the activity yield differences between the analytical and MC profiles were evaluated using the normalized root-mean-square error (NRMSE).

2.5.1. MLS method

The MLS method was originally proposed by Frey *et al* (2014) for offline PET-based treatment monitoring and widely used in in-vivo PET verification (Zhang *et al* 2021, Moglioni *et al* 2022). For each pair of coordinates (x, y) in the transverse plane, it takes 1D activity profiles along the beam direction from the two 3D activity distributions to be compared and calculates the most likely shift δ_{MLS} that minimizes the difference between a distal fall-off segment of the two profiles:

$$\delta R_{MLS} = \arg\min_{\delta_{MLS}} \left(\sum_{z_{min}}^{z_{max}} \left| A_{ref}(z) - A_{pred}(z - \delta_{MLS}) \right| \right) \tag{2}$$

where A_{ref} and A_{pred} represent the reference (i.e. simulated or measured) and the analytically predicted activity profiles, respectively. We applied the method exactly as described in Frey *et al* (2014). The parameters z_{min} and z_{max} define the distal region of interest: z_{max} is the maximum depth between the 50% dose fall-off and the 20% activity fall-off, and z_{min} ranges from the location of the activity maximum and one voxel upstream of z_{max}. Moreover, only those profiles with an integrated activity of at least 20% of the highest integrated activity were considered, so that low activity profiles, known for being less reliable (Min *et al* 2013, Frey *et al* 2014), are excluded from analysis. For a detailed description, the reader is referred to Frey *et al* (2014).

3. Results

Figure 1 shows MC-simulated dose-to-water distributions from our simulations and from HIT for all patient cases. Gamma index passing ratios of 99.97%, 99.92%, 99.50% and 99.35% (1%/1 mm criteria with 10% maximum threshold) for the BR, HN, LIV and PEL cases, respectively, demonstrate good consistency of simulations between the Geant4-based platform and HIT data, enabling the use of the simulated dose of each spot for the analytical predictions.

Figure 2 shows results for the BR case. Comparing the analytical/MC-simulated results before and after washout effect correction (figure 2(a) vs. (c)/(b) vs. (d)) shows that most activity initially formed in the brain was washed away, leading to two separate areas of stronger activation in the upstream skull region and in the downstream tumor region. Figure 2(e) shows the measured PET image where the local maximum in the bone (ca. 8 Bq ml^{-1}) is much lower than the one in the distal tumor (ca. 30 Bq ml^{-1}), mainly contributed by the stopping projectile PEs. 1D profiles extracted along the white line will be displayed later to better reveal both peaks.

Figure 3 shows results for the HN case. A similar washout effect can be observed for the HN case when comparing (a) with (c) and (b) with (d), where the activity in soft tissue decreases and the main activity is located at the distal region in front of the spinal cord. The measured PET likewise exhibits a local maxima in this distal region, mainly contributed by the projectile PEs (see figure 3(e)).

Figures 4 and 5 show results for the LIV and PEL cases, respectively. In figure 4, two parallel irradiation fields were used. Again, a comparison of the analytical and MC results before and after washout correction indicates that activity initially formed in the liver was largely reduced, leaving local activity maxima in the entering fat region and distal tumors. These features also appear in the measured PET

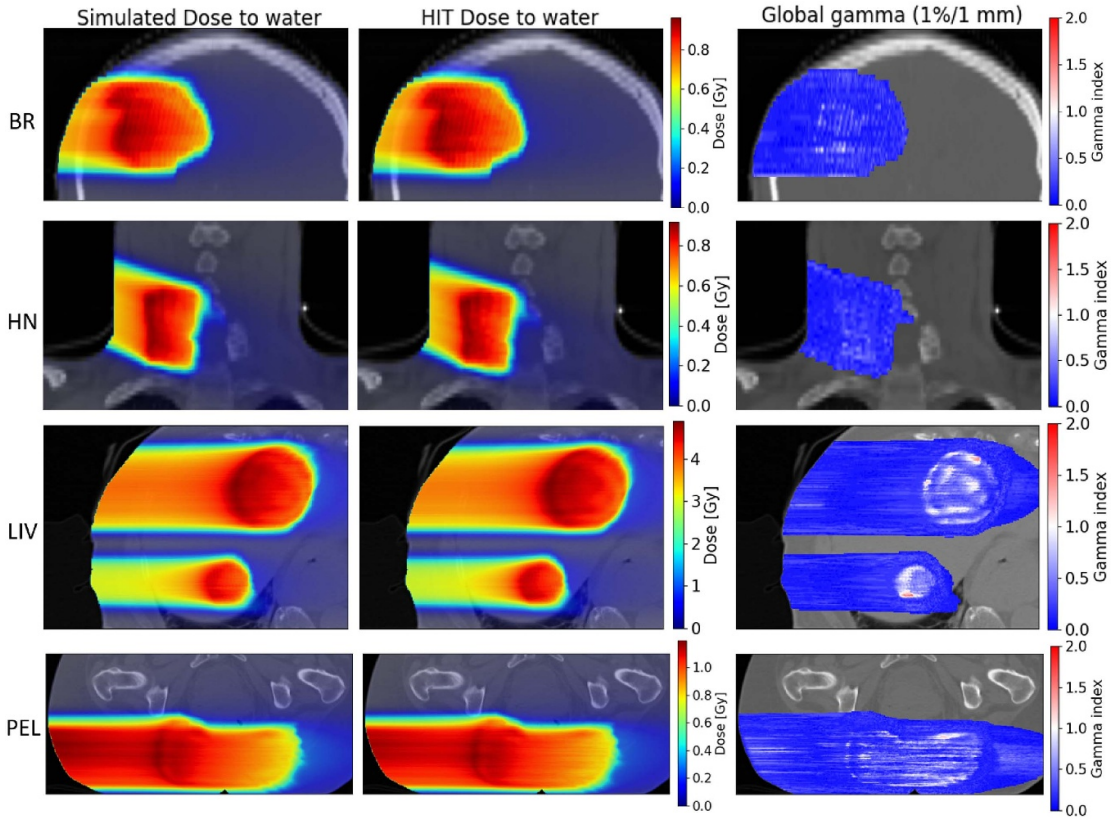

Figure 1. Consistency check of dose-to-water between our Geant4 MC simulations and HIT FLUKA MC. Dose-to-water distributions of the BR, HN, LIV and PEL cases from top to bottom, calculated using the Geant4-based platform developed for this work (left) and by HIT (middle), along with gamma index maps (right), using 1%/1 mm criteria, overlaid onto the corresponding planning CT images.

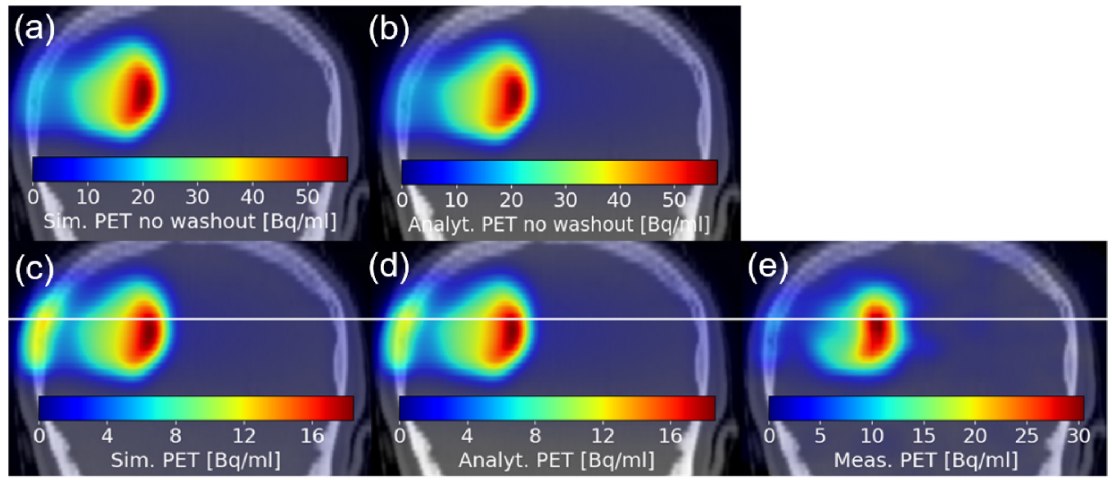

Figure 2. Results for the BR case displayed in coronal view. Geant4 MC-simulated PET images are shown in (a) and (c); analytical PET images in (b) and (d); measured PET in (e). (a) and (b) are displayed PET without washout correction, whereas (c) and (d) include washout correction. The white lines in (c)–(e) indicate where the profiles along the beam direction were extracted.

image (figure 4(e)). Similarly, in figure 5, the washout effect reduces activity in muscle tissue, with the main activity remaining in body fat and the distal region. Figure 5(e) exhibits the local activity maxima at the distal region similar to those in (c) and (d), but shows the noisiest measured PET result among the four cases.

For all the four cases, analytical predicted PET images closely match simulated results in shape and amplitude based on figure 2–5. However, differences to the measured PET images are observed, with a similar level of disagreement for both analytical and simulated results, primarily due to inaccuracies in

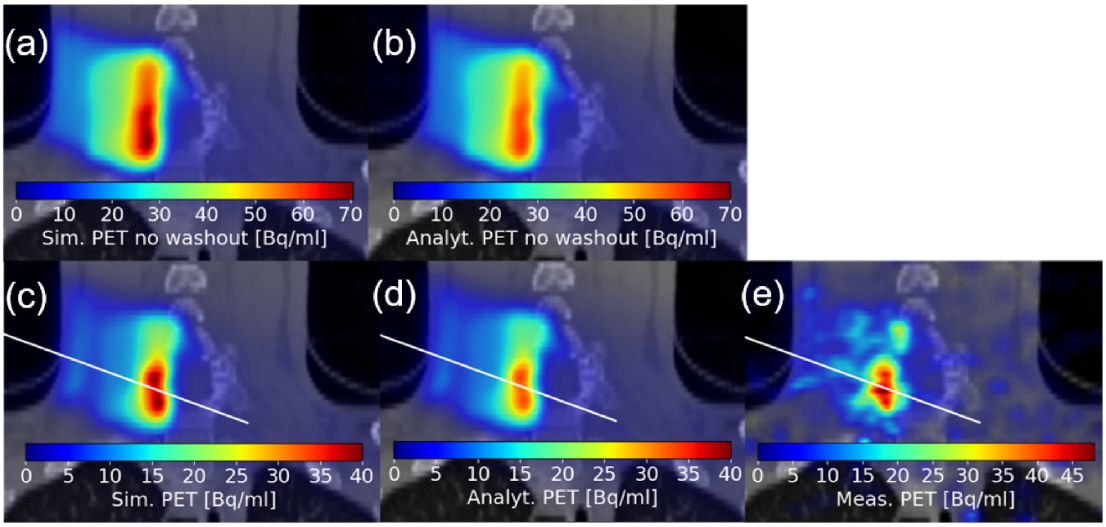

Figure 3. Results for the HN case displayed in coronal view. Geant4 MC-simulated PET images are shown in (a) and (c); analytical PET images in (b) and (d); measured PET in (e). (a) and (b) are displayed PET without washout correction, whereas (c) and (d) include washout correction. The white lines in (c)–(e) indicate where the profiles along the beam direction were extracted.

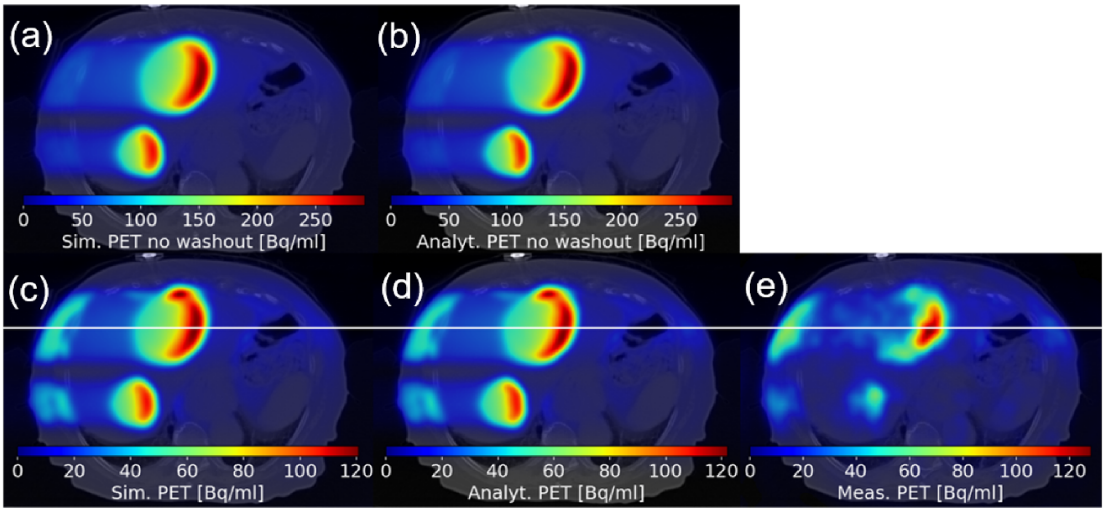

Figure 4. Results for the LIV case displayed in axial view. Geant4 MC-simulated PET images are shown in (a) and (c); analytical PET images in (b) and (d); measured PET in (e). (a) and (b) are displayed PET without washout correction, whereas (c) and (d) include washout correction. The white lines in (c)–(e) indicate where the profiles along the beam direction were extracted.

the washout effect correction and noise in measured PET data (Bauer *et al* 2013, Frey *et al* 2014, Kurz *et al* 2016), but also to an additional effect related to the temporal structure of the scanning beam delivery, which was not explicitly modeled in the current framework and was assumed to be negligible compared to the delay between irradiation and PET acquisition. Nevertheless, the maxima positions among the analytical, simulated, and measured PET images remain qualitatively well aligned.

To confirm this observation, 1D activity profiles were extracted along the white lines shown in figures 2–5. A quantitative comparison of selected activity profiles with corresponding CT values is shown in figure 6. For the brain case (figure 6(a)), analytical and MC simulated PET profiles show excellent agreement in shape and amplitude, with consistent peak positions in the bone and distal regions compared to measurements. The measured activity in the tumor volume is significantly higher than expected, which suggests an overestimated washout correction in the tumor volume.

For the head/neck case (figure 6(b)), the analytical prediction underestimates the distal activity peak relative to the MC simulation. This discrepancy can be attributed to the pronounced tissue heterogeneity at that region, as evident from the CT profile. Spatial agreement is observed between the predicted and measured activity gradients near the spinal cord structure.

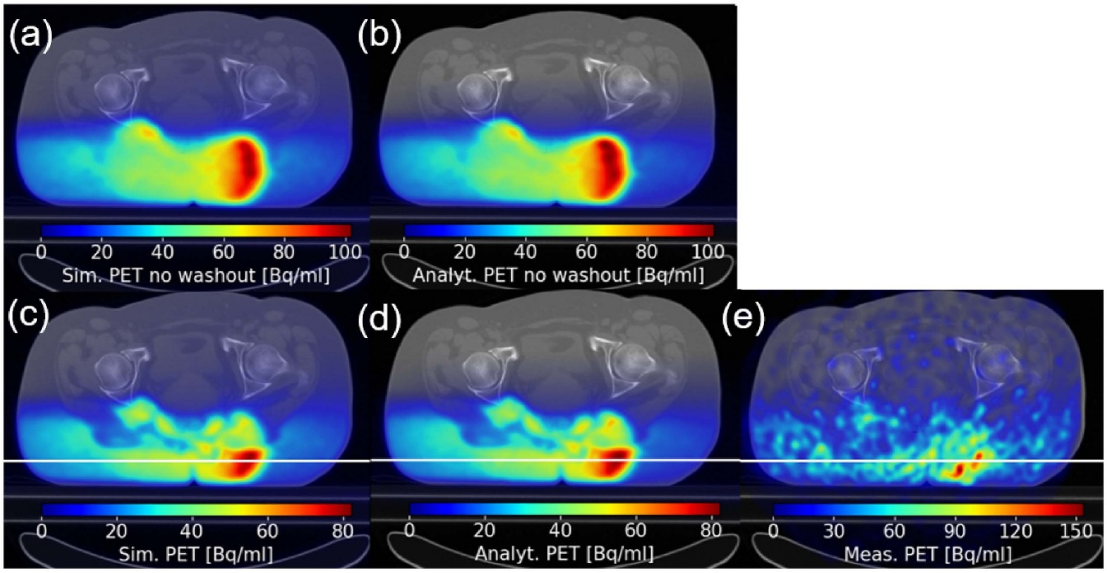

Figure 5. Results for the PEL case displayed in axial view. Geant4 MC-simulated PET images are shown in (a) and (c); analytical PET images in (b) and (d); measured PET in (e). (a) and (b) are displayed PET without washout correction, whereas (c) and (d) include washout correction. The white lines in (c)–(e) indicate where the profiles along the beam direction were extracted.

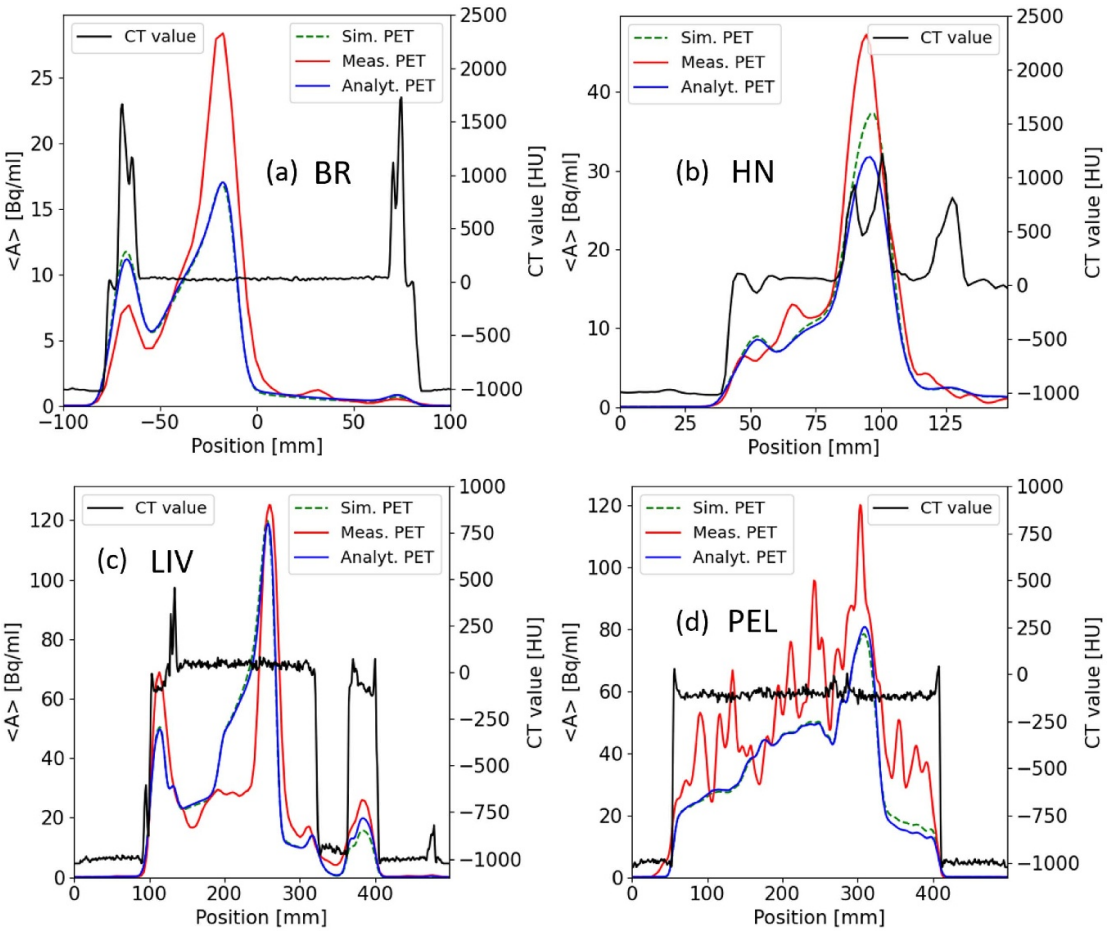

Figure 6. Selected depth activity-profiles along the white lines in figures 2–5 with corresponding CT values are shown in (a)–(d) for the BR, HN, LIV, and PEL cases, respectively.

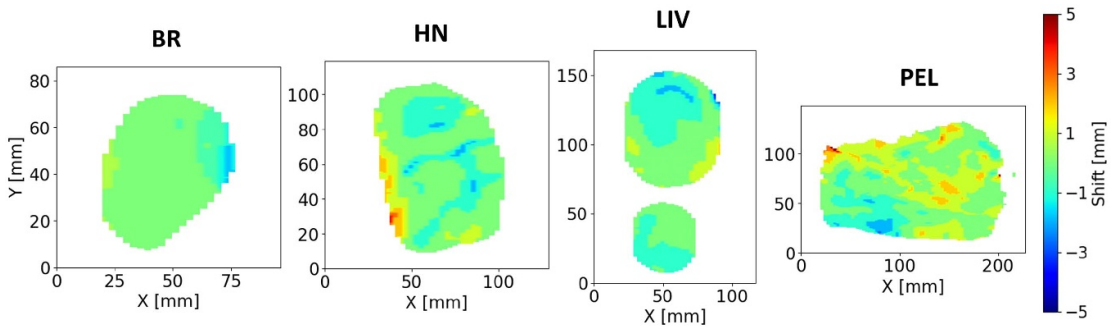

Figure 7. Range shift maps for BR, HN, LIV and PEL from left to right using the MLS method. Analytical and simulated distributions are compared.

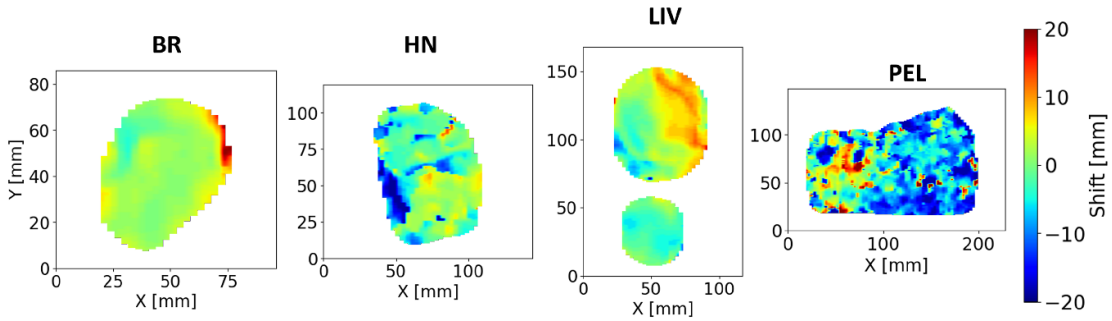

Figure 8. Range shift maps for BR, HN, LIV and PEL from left to right using the MLS method. Analytical and measured distributions are compared.

For the liver case (figure 6(c)), analytical and MC simulated PET profiles also show strong agreement, with a minor discrepancy in the distal fat region behind the air cavity. Three peaks in the entering fat region, at the tumor, and in the distal fat region are observed in both analytical and measured profiles, and they share close peak positions.

For the pelvic case (figure 6(d)), analytical and MC simulated PET profiles again demonstrate excellent agreement in shape and amplitude. It is hard to identify peaks from the noisy measured profile, while one peak can be identified in the analytical profile and its distal fall-off closely corresponds to the distal fall-off of the highest peak in the measured profile.

The MLS method presented in section 2.5 was used to quantify the range deviation between the analytical activity distribution and the simulated or measured results in beam-eye-view (BEV). Figure 7 shows the range differences between the analytical and the simulated activity distributions in BEV by the MLS method for the BR, HN, LIV and PEL cases from left to right.

We calculated the mean range differences and their root-mean-square error (RMSD), as listed in the first row of table 3. The range deviation between the analytical and simulated activity distributions in all four cases remain below 0.5 mm, with all RMSD values under 1 mm. It demonstrates excellent range agreement between our analytical predictions and the MC simulations for the four cases. The activity yield differences between the analytical and MC profiles are evaluated using NRMSE. The third row of table 3 shows the mean NRMSE values and corresponding RMSD values. The HN and PEL cases exhibit slightly higher mean NRMSE, mainly due to the complex heterogeneities and larger noise in PET images caused by stronger tissue attenuation and reduced photon detection in head-and-neck and pelvic regions. Overall, the mean NRMSE values ranged between 1%–2% and the RMSD values are below 1%, demonstrating that our analytical approach predicts the distribution amplitudes with a comparable accuracy as the MC simulations.

Figure 8 shows the range differences between the analytical and the measured activity distributions in BEV by the MLS method for the BR, HN, LIV and PEL cases from left to right. For the HN and PEL cases, the shift maps show numerous regions with large shifts of –10 to –20 mm, compared to BR and LIV cases. This is primarily due to the greater statistical noise and fluctuations in the measured PET data

Table 3. Mean range differences (Shifts) and mean NRMSE with corresponding RMSD values for BR, HN, LIV, and PEL. Rows in italics refer to analytical vs. measured distributions; the remaining rows refer to analytical vs. simulated distributions.

	BR	HN	LIV	PEL
Shifts (mm)	-0.11 ± 0.40	-0.08 ± 0.77	-0.35 ± 0.67	0.25 ± 0.88
	2.36 ± 3.23	*–2.29 ± 6.10*	*1.57 ± 4.88*	*–5.46 ± 8.71*
NRMSE (%)	1.25 ± 0.51	1.54 ± 0.44	1.25 ± 0.48	2.04 ± 0.83
	—	—	—	—

Note: NRMSE is not reported for the analytical vs. measured comparison due to the higher noise level in measured PET profiles.

for HN and PEL (cf figures 3(e) and 5(e)). The MLS method compares a dynamically selected distal segment of the measured profile to the corresponding segment of the analytical profile. When the measured data are noisy, the resulting shape mismatch can be too large for a realistic MLS to exist. The mean range differences and their RMSD are listed in the second row of table 3. Overall, the mean deviations are within ± 3 mm excluding the PEL case. Figure 8 highlights several regions where the shifts between the analytical prediction and the measured PET exceed ± 10 mm: positive shifts along the right edge of BR, negative shifts along the left side of HN, positive shifts at the upper part of LIV, and for PEL, positive shifts on the left side and negative shifts on the right, top, and bottom edges. A definitive explanation of these large shift regions would require a dedicated deformable-registration analysis between the planning CT and the CT acquired on the day of the PET/CT, which is beyond the purpose of the present validation study. Nevertheless, same or similar cases have been reported in previous PET-based range-verification studies (e.g. Bauer *et al* 2013, and their relevant findings and explanations will be discussed in the section 4.

4. Discussion and conclusion

This work validated an in-house developed analytical approach for in-vivo PET verification in carbon ion therapy using four patients cases in real clinical conditions. The validation followed a multi-stage strategy. First, our MC simulations were tuned to reproduce the HIT MC dose calculation, which is considered the gold standard and was used to create HIT TPS database. Next, the consistency between our MC and the HIT MC dose-to-water was verified. Once validated, our MC simulations were used as the gold-standard reference to assess the analytical predicted PET images, given that the analytical predictions were based on MC-simulated dose-to-tissue distributions and the parameters of the approach were derived by fitting MC-calculated data (Du *et al* 2025). The good agreement between the analytical predictions and MC simulations (with mean longitudinal shifts $\leqslant 0.5$ mm and mean NRMSE values $\leqslant 2\%$) confirms that our method accurately predicts PED in terms of both range and amplitude. The longitudinal shifts between the analytical predictions and measured data were subsequently evaluated. A direct investigation of the reason of shifts between analytical predictions and measured PET images was beyond the scope of this work, as these patient data had already been analyzed in previous PET-based range verification studies at HIT. Therefore, we refer to these studies for the interpretation of such deviations.

Bauer *et al* (2013) reported the same BR and HN cases. Rather than analyzing range shift maps, the study compared activity profiles along the beam direction, similar to that shown in figure 6, and found good spatial agreement between the predicted and measured activity and deemed them a proper beam delivery. Moreover, Nischwitz *et al* (2015) investigated 10 patients with primary glioblastoma and reported two representative cases in detail. The first case featured a small, relatively homogeneous tumor. Its range shift map showed overall low range deviation with a few large deviations (ca. 10 mm) along the left edge and yielded an average MLS of 1.9 ± 2.2 mm. The second case was a large tumor of complex, irregular shape with a central necrosis and surrounding oedema. The range shift map revealed a broader region of pronounced shifts (upper-left) and a mean MLS of 6.4 ± 5.2 mm. Nischwitz *et al* (2015) concluded that the beam range in homogeneous tumors was more accurate than in inhomogeneous ones, which explained the larger shift of their second case. Besides, Nischwitz *et al* (2015) noted that being below the used safety margins of commonly 3–5 mm, allow a solid prediction of the beam range. Our BR case with few large shifts at the upper-left edge has a mean MLS of 2.36 ± 3.23 mm, which falls into

this interval. This result supports the reliability of our range prediction and also confirms a proper beam delivery, as also concluded by Bauer *et al* (2013).

Kurz *et al* (2016) reported the same LIV case. A 5–20 mm region of over-range in figure 8(L)IV) was also noted in the corresponding range shift map. This deviation was attributed to slight differences in the patient's outer contour on the treatment day, in addition to residual motion despite the application of an abdominal press (Kurz *et al* 2016). In addition, Kurz *et al* (2016) reported a mean MLS of 1.56 ± 4.57 mm between measured data and simulation which closely aligns with our result of 1.57 ± 4.88 mm. The similar range shift map and nearly identical mean MLS value confirm the accuracy of our range prediction for the LIV case.

Frey *et al* (2014) reported one pelvic case (different from our PEL), and a pronounced continuous over-range region was displayed in their range shift map which was confirmed to be an overshoot due to the anatomic changes between planning CT and actual patient positioning for treatment delivery. This resulted in a mean MLS of 4.26 ± 11.25 mm. As a consequence, the simulation was redone based on the CT obtained from the PET/CT scan after the treatment. The pronounced over-range region disappeared, and the corresponding MLS analysis showed a good conformity of the two distributions, yeilding a mean MLS of 0.71 ± 8.34 mm. In comparison, the range shift map for our PEL case shows large shift regions that are relatively scattered across the field, without any continuous and pronounced area. Given that the PET image for PEL is already the noisiest among the four cases (see figure 5(d)), we cannot rule out a significant influence of image noise associated with low counting statistics and/or inaccuracies in the biological washout model on the observed range differences.

A different approach for 3D PED calculations in carbon ion therapy based on a database of PET yields measured in phantoms was proposed and validated with a patient case by Helmbrecht *et al* (2016). A thorough comparison was previously made in Du *et al* (2025) and showed that our method provided better range prediction than the approach of Helmbrecht *et al* (2016). However, a key advantage of their technique is that it relied on experimental yield data and avoided any potential inaccuracies in the MC-based data introduced by physics models or cross-section data. From this perspective, our method is limited by the accuracy of MC simulations needed for but would also benefit from ongoing advancements in physics models and cross-section databases (Horst *et al* 2019, Mancini-Terracciano *et al* 2019, Sato *et al* 2022, Gao *et al* 2023).

Our analytical method achieves accurate range predictions compared to MC simulations with a higher computational speed. Although the code is a proof-of-principle version and can be further optimized, it already performs about 40 times faster than CPU-based MC tools (Du *et al* 2025). In addition, it relies on a traditional PBA and employs a data structure similar to that used by standard TPS, facilitating straightforward integration into clinical workflows. As demonstrated for proton therapy using a filtering-based approach (Frey *et al* 2013, Pinto *et al* 2020), this method can potentially enable range predictions shortly after the end of treatment in offline PET monitoring. Moreover, our method allows for fine tuning of the predicted yields by applying an isotope-specific scaling factor once the MC engine is calibrated to a given facility or experimental yield data become available.

As Frey *et al* (2014) noted and our study also demonstrated, inaccuracies in the biological washout model and image noise from low counting statistics also lead to range discrepancies between measurements and predictions. The PET data used in this work were acquired more than 10 years ago using a back then state-of-the-art full-ring PET/CT scanner. As only a limited number of centers have performed PET-based range verification in carbon ion therapy, such datasets remain scarce. Besides, in this study, we specifically focused on PET datasets acquired with a full-ring PET system, which allows avoiding additional complexities related to detector response modeling and instead focus on the prediction of the PED themselves. This is in contrast to other PET system designs (e.g. dual-head configurations), where accurate modeling of the detector system becomes an additional source of uncertainty. However, these data are affected by inherent limitations, including low counting statistics due to the offline acquisition protocol and, particularly in the pelvic region, increased attenuation resulting from the larger patient thickness. The challenges of reliably reconstructing broad activity distributions at low count rates for this scanner have also been reported in previous studies (Kurz *et al* 2015).

Ongoing research on biological washout in animals (Helmbrecht *et al* 2013, Ammar *et al* 2014, Toramatsu *et al* 2018, 2022, 2023) aims to improve the modeling of these washout effects. Novel PET reconstruction methods (Kurz *et al* 2016, Reader *et al* 2020, Xie *et al* 2021, Hashimoto *et al* 2024) could also help improve image quality. Additionally, in-beam PET, which is less affected by washout-induced signal degradation, can offer higher image accuracy (Dendooven *et al* 2015, Ferrero *et al* 2018, Fiorina *et al* 2021, Tashima *et al* 2023, Kraan *et al* 2024). In future work, we plan to validate the method using data acquired with in-beam PET (in particular using full-ring PET scanners), as in-beam PET represents

the most promising form of *in vivo* treatment verification during beam delivery in modern carbon ion therapy.

Acknowledgments

We would like to express our gratitude to Prof. Jürgen Debus from HIT for agreeing to share the patient data. This work has received financial support from the China Scholarship Council (CSC) and Ludwig-Maximilians-Universität München (LMU).

Data availability statement

The data cannot be made publicly available upon publication because they are owned by a third party and the terms of use prevent public distribution. The data that support the findings of this study are available upon reasonable request from the authors.

Author contributions

Tianxue Du 0009-0008-9539-8547
Conceptualization (equal), Formal analysis (lead), Methodology (lead), Validation (lead), Visualization (lead), Writing – original draft (lead), Writing – review & editing (equal)

Julia Bauer
Resources (supporting), Writing – review & editing (supporting)

Thomas Tessonnier 0000-0002-8919-4299
Resources (supporting), Writing – review & editing (supporting)

Katia Parodi 0000-0001-7779-6690
Funding acquisition (supporting), Resources (equal), Supervision (equal), Writing – review & editing (equal)

Marco Pinto 0000-0001-6835-2561
Supervision (equal), Writing – review & editing (equal)

Appendix. 1D analytical approach for IDPED construction

Hofmann *et al* (2019) adopted a filter-based approach proposed by Parodi and Bortfeld (2006) for predicting positron emitter distributions (PED) along the beam path in proton therapy by convolving the dose profile $D(z)$ with a filter $f(z)$.

$$P(z) = D(z) * f(z) = \int_{-\infty}^{\infty} D(z')f(z-z')\,\mathrm{d}z'. \tag{A.1}$$

They extended this approach to carbon ion therapy and found the filter highly energy-dependent, which did not reproduce the PED when applied to other energies. Consequently, they used the distal fall-off positions of the convolved profile to locate the PED, while the shape was reconstructed using parameterized modeling functions (Hofmann *et al* 2019). Following closely their method, we developed an enhanced 1D analytical approach with finer modeling functions, and consideration of more PEs channels (Du *et al* 2025).

The integrated depth PED (IDPED) of the target PEs, generated in the reference material, are described as having a build-up part followed by a distal part (Hofmann *et al* 2019, Du *et al* 2025). An example of the IDPED for the $^{11}C_{target}$ is shown in figure A1. An analytical function, comprising the sum of two exponential terms, was used to describe the build-up part b for each target PE subspecies i:

$$\mathrm{IDPED}_{i,b}(E,z) = A_i\left[1-\alpha_i\exp\left(-c_{1,i}z\right)\right] + B_i\left[\exp\left(c_{2,i}z\right)-1\right], \tag{A.2}$$

where the first one describes a less steep build-up and the other one compensates for the rapid growth in the area just before the Bragg peak, A_i is the theoretical maximum number of produced PE at large

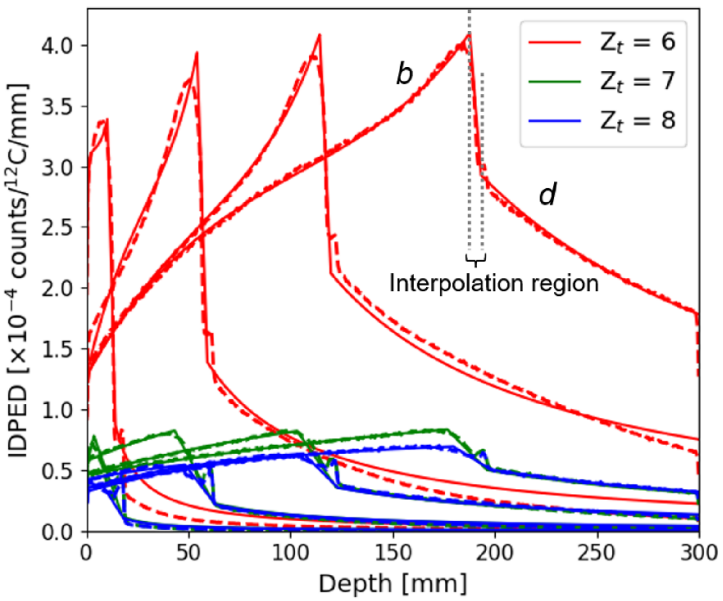

Figure A1. IDPED for the $^{11}C_{target}$ generated from the interactions of ^{12}C ion beams of initial kinetic energies of 100, 200, 300 and 400 MeV/n with carbon (red), nitrogen (green) and oxygen (blue) target nuclei in the reference material. The MC simulated IDPEDs are shown in dashed and the analytical IDPEDs are shown in solid lines. Two gray vertical lines separate the red solid line, representing the analytical IDPED for $^{11}C_{target}$ with carbon target of 400 MeV/n, into three regions: the build-up region *b*, the interpolation region and the distal region *d*, from left to right.

depth from the less steep build-up, α_i is determined by the number of PE at the entrance of phantom, $c_{1,i}$ is considered as the build-up rate, B_i is determined by the difference in the number of PE at the end of build-up predicted by the first exponential term and the one obtained from Monte Carlo (MC) simulation, and $c_{2,i}$ represents the rate of the rapid growth.

For the distal part d of IDPED, a power function correlated with the initial kinetic energy E of the carbon ion beam was proposed:

$$\mathrm{IDPED}_{i,d}(E,z) = \beta_i E^3 \frac{1}{z^{n_i}}, \tag{A.3}$$

where a scaling factor β_i and the power of function n_i depend on the type of PE denoted as i and are both energy-independent. The gap between the end of build-up part and beginning of distal part is interpolated linearly.

The modeling functions for the IDPED for projectile PEs, except those generated from target hydrogen nuclei, follows closely what was described by Hofmann *et al* (2019). The distal limit of IDPED was first predicted by the 80% distal fall-off position of convolved profiles P. The proximal limit was then determined by the ratio $\frac{A_f}{A_p}$ of the incident primary particle range, with $A_{p,f}$ being the mass numbers of the primary particle and the fragments, respectively. The incident particle range was determined by the 80% distal fall-off position of IDD. Finally, the analytical function predicting the IDPED profile for each subspecies of projectile PEs i was given by

$$\mathrm{IDPED}_{i,\mathrm{proj}}(E,z) = \{h_i(E) \cdot \Phi_{^{12}C}(z)\} * G_i(z), \tag{A.4}$$

where $h_i(E)$ is an energy-dependent scaling factor in the form of a fourth-degree polynomial to account for the height of the IDPED peak, $\Phi_{^{12}C}(z)$ is the fluence loss correction for ^{12}C and the Gaussian function $G_i(z)$ accounts for energy loss fluctuations. The analytical IDPED of four energies are shown in solid lines in figure A2, with a comparison to the simulated results in dashed lines.

As for the IDPED for $^{11}C_{proj}$ and $^{10}C_{proj}$ from target hydrogen nuclei, i.e. the yellow dashed profiles shown in figure A2, we found that a Landau distribution provides a better fit. The modeling function is provided below:

$$\mathrm{IDPED}(E,z) = \{k(E) \cdot \mathrm{Landau}(\mu,\eta)\} * G(z), \tag{A.5}$$

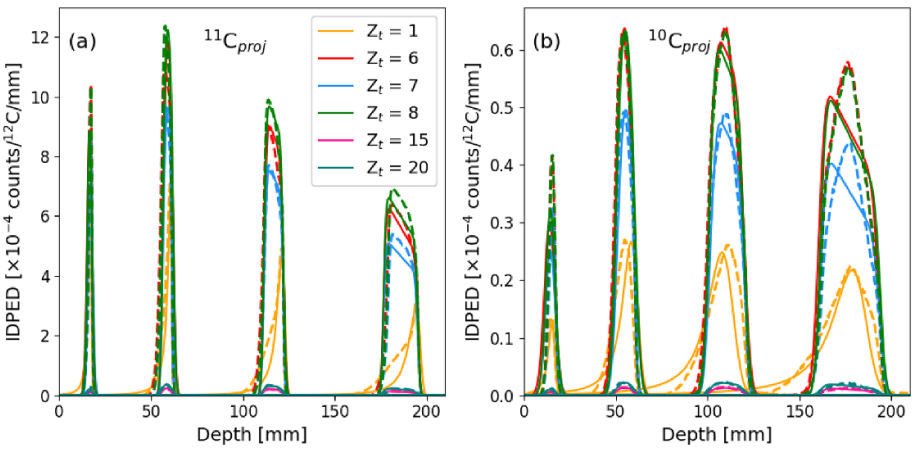

Figure A2. IDPED for the two projectile PEs, (a) $^{11}C_{proj}$, (b) $^{10}C_{proj}$ generated from the interactions of ^{12}C ion beams of initial kinetic energies of 100, 200, 300 and 400 MeV/n with the six different target nuclei in the reference material. The MC simulated IDPEDs are shown in dashed lines and the analytical IDPEDs are shown in solid lines.

where $k(E)$ is an energy-dependent scaling parameter in the form of a three-degree polynomial, μ is the maximum position of the Landau distribution determined by the maximum position of convolved profiles P, η is the width parameter of the Landau distribution, which shows a linear correlation to the 80% distal fall-off position of integrated depth dose, and a Gaussian term $G(z)$ accounts for energy loss fluctuations. The fitting results are shown by the yellow solid profiles in figure A2.

References

Agostinelli S *et al* 2003 GEANT4—a simulation toolkit *Nucl. Instrum. Methods Phys. Res. A* **506** 250–303

Ammar C *et al* 2014 Comparing the biological washout of β+-activity induced in mice brain after 12C-ion and proton irradiation *Phys. Med. Biol.* **59** 7229

Bauer J *et al* 2014 Integration and evaluation of automated Monte Carlo simulations in the clinical practice of scanned proton and carbon ion beam therapy *Phys. Med. Biol.* **59** 4635

Bauer J, Unholtz D, Sommerer F, Kurz C, Haberer T, Herfarth K, Welzel T, Combs S E, Debus J and Parodi K 2013 Implementation and initial clinical experience of offline PET/CT-based verification of scanned carbon ion treatment *Radiother. Oncol.* **107** 218–26

Borys D *et al* 2022 ProTheRaMon—a GATE simulation framework for proton therapy range monitoring using PET imaging *Phys. Med. Biol.* **67** 224002

Chacon A *et al* 2019 Comparative study of alternative Geant4 hadronic ion inelastic physics models for prediction of positron-emitting radionuclide production in carbon and oxygen ion therapy *Phys. Med. Biol.* **64** 155014

Chacon A *et al* 2024 A quantitative assessment of Geant4 for predicting the yield and distribution of positron-emitting fragments in ion beam therapy *Phys. Med. Biol.* **69** 125015

Choi K, Mein S B, Kopp B, Magro G, Molinelli S, Ciocca M and Mairani A 2018 FRoG—a new calculation engine for clinical investigations with proton and carbon ion beams at CNAO *Cancers* **10** 395

Combs S E, Bauer J, Unholtz D, Kurz C, Welzel T, Habermehl D, Haberer T, Debus J and Parodi K 2012 Monitoring of patients treated with particle therapy using positron-emission-tomography (PET): the MIRANDA study *BMC Cancer* **12** 1–6

Dendooven P, Buitenhuis H, Diblen F, Heeres P, Biegun A, Fiedler F, Van Goethem M, Van der Graaf E and Brandenburg S 2015 Short-lived positron emitters in beam-on PET imaging during proton therapy *Phys. Med. Biol.* **60** 8923

Du T, Bauer J, Parodi K and Pinto M 2025 An analytical approach to predict 3D positron emitter distribution in carbon ion therapy *Phys. Med. Biol.* **70** 145027

Ferrero V *et al* 2018 Online proton therapy monitoring: clinical test of a Silicon-photodetector-based in-beam PET *Sci. Rep.* **8** 4100

Fiorina E *et al* 2021 Detection of interfractional morphological changes in proton therapy: a simulation and *in vivo* study with the INSIDE in-beam PET *Front. Phys.* **8** 578388

Frey K, Bauer J, Unholtz D, Kurz C, Krämer M, Bortfeld T and Parodi K 2013 TPS_PET—A TPS-based approach for *in vivo* dose verification with PET in proton therapy *Phys. Med. Biol.* **59** 1

Frey K, Unholtz D, Bauer J, Debus J, Min C H, Bortfeld T, Paganetti H and Parodi K 2014 Automation and uncertainty analysis of a method for in-vivo range verification in particle therapy *Phys. Med. Biol.* **59** 5903–19

Gao Z, Zhang X, Zhang Y, Ju Y, Chen L, Ge H, Ma F, Chen Z and Yang W 2023 Benchmarking GEANT4 nuclear models for light fragments of 80.5 MeV/u carbon ions bombarding heavy-metal targets *Phys. Rev. C* **107** 064618

Hashimoto F, Onishi Y, Ote K, Tashima H, Reader A J and Yamaya T 2024 Deep learning-based PET image denoising and reconstruction: a review *Radiol. Phys. Technol.* **17** 24–46

Helmbrecht S, Enghardt W, Parodi K, Didinger B, Debus J, Kunath D, Priegnitz M and Fiedler F 2013 Analysis of metabolic washout of positron emitters produced during carbon ion head and neck radiotherapy *Med. Phys.* **40** 091918

Helmbrecht S, Priegnitz M, Enghardt W, Rohling H and Fiedler F 2016 Application of a yield approach for the prediction of positron emitter distributions produced during therapeutic carbon-ion beam irradiation *IEEE Trans. Nucl. Sci.* **63** 61–69

Hofmann T, Fochi A, Parodi K and Pinto M 2019 Prediction of positron emitter distributions for range monitoring in carbon ion therapy: an analytical approach *Phys. Med. Biol.* **64** 105022
Horst F *et al* 2019 Measurement of PET isotope production cross sections for protons and carbon ions on carbon and oxygen targets for applications in particle therapy range verification *Phys. Med. Biol.* **64** 205012
Jia X, Schümann J, Paganetti H and Jiang S B 2012 GPU-based fast Monte Carlo dose calculation for proton therapy *Phys. Med. Biol.* **57** 7783
Kraan A C *et al* 2024 In-beam PET treatment monitoring of carbon therapy patients: Results of a clinical trial at CNAO *Phys. Medica* **125** 104493
Kurz C, Bauer J, Conti M, Guérin L, Eriksson L and Parodi K 2015 Investigating the limits of PET/CT imaging at very low true count rates and high random fractions in ion-beam therapy monitoring *Med. Phys.* **42** 3979–91
Kurz C, Bauer J, Unholtz D, Richter D, Herfarth K, Debus J and Parodi K 2016 Initial clinical evaluation of PET-based ion beam therapy monitoring under consideration of organ motion *Med. Phys.* **43** 975–82
Lysakovski P, Kopp B, Tessonnier T, Mein S, Ferrari A, Haberer T, Debus J and Mairani A 2024 Development and validation of monteray, a fast Monte Carlo dose engine for carbon ion beam radiotherapy *Med. Phys.* **51** 1433–49
Malouff T D, Mahajan A, Krishnan S, Beltran C, Seneviratne D S and Trifiletti D M 2020 Carbon ion therapy: a modern review of an emerging technology *Front. Oncol.* **10** 82
Mancini-Terracciano C, Asai M, Caccia B, Cirrone G, Dotti A, Faccini R, Napolitani P, Pandola L, Wright D and Colonna M 2019 Preliminary results coupling "Stochastic Mean Field" and "Boltzmann-Langevin One Body" models with Geant4 *Phys. Medica* **67** 116–22
McNamara K *et al* 2022 GPU accelerated Monte Carlo scoring of positron emitting isotopes produced during proton therapy for PET verification *Phys. Med. Biol.* **67** 244001
Min C H, Zhu X, Winey B A, Grogg K, Testa M, Fakhri G E, Bortfeld T R, Paganetti H and Shih H A 2013 Clinical application of in-room positron emission tomography for *in vivo* treatment monitoring in proton radiation therapy *Int. J. Radiat. Oncol.* Biol.* Phys.* **86** 183–9
Mizuno H *et al* 2003 Washout measurement of radioisotope implanted by radioactive beams in the rabbit *Phys. Med. Biol.* **48** 2269
Moglioni M *et al* 2022 In-vivo range verification analysis with in-beam PET data for patients treated with proton therapy at CNAO *Front. Oncol.* **12** 929949
Nischwitz S P *et al* 2015 Clinical implementation and range evaluation of *in vivo* PET dosimetry for particle irradiation in patients with primary glioma *Radiother. Oncol.* **115** 179–85
Oelfke U, Lam G and Atkins M 1996 Proton dose monitoring with PET: quantitative studies in lucite *Phys. Med. Biol.* **41** 177
Pönisch F, Parodi K, Hasch B G and Enghardt W 2004 The modelling of positron emitter production and PET imaging during carbon ion therapy *Phys. Med. Biol.* **49** 5217
Parodi K *et al* 2007 Patient study of *in vivo* verification of beam delivery and range, using positron emission tomography and computed tomography imaging after proton therapy *Int. J. Radiat. Oncol.* Biol.* Phys.* **68** 920–34
Parodi K and Bortfeld T 2006 A filtering approach based on Gaussian-powerlaw convolutions for local PET verification of proton radiotherapy *Phys. Med. Biol.* **51** 7089–106
Parodi K, Mairani A, Brons S, Hasch B G, Sommerer F, Naumann J, Jäkel O, Haberer T and Debus J 2012 Monte Carlo simulations to support start-up and treatment planning of scanned proton and carbon ion therapy at a synchrotron-based facility *Phys. Med. Biol.* **57** 3759–84
Parodi K, Mairani A and Sommerer F 2013 Monte Carlo-based parametrization of the lateral dose spread for clinical treatment planning of scanned proton and carbon ion beams *J. Radiat. Res.* **54** i91–i96
Parodi K, Paganetti H, Cascio E, Flanz J B, Bonab A A, Alpert N M, Lohmann K and Bortfeld T 2007 PET/CT imaging for treatment verification after proton therapy: a study with plastic phantoms and metallic implants *Med. Phys.* **34** 419–35
Parodi K, Ponisch F and Enghardt W 2005 Experimental study on the feasibility of in-beam PET for accurate monitoring of proton therapy *IEEE Trans. Nucl. Sci.* **52** 778–86
Pennazio F *et al* 2018 Carbon ions beam therapy monitoring with the INSIDE in-beam PET *Phys. Med. Biol.* **63** 145018
Pinto M, Kröniger K, Bauer J, Nilsson R, Traneus E and Parodi K 2020 A filtering approach for PET and PG predictions in a proton treatment planning system *Phys. Med. Biol.* **65** 095014
Priegnitz M, Fiedler F, Kunath D, Laube K and Enghardt W 2012 An experiment-based approach for predicting positron emitter distributions produced during therapeutic ion irradiation *IEEE Trans. Nucl. Sci.* **59** 77–87
Reader A J, Corda G, Mehranian A, da Costa-Luis C, Ellis S and Schnabel J A 2020 Deep learning for PET image reconstruction *IEEE Trans. Radiat. Plasma Med. Sci.* **5** 1–25
Sato Y-h, Sakata D, Bolst D, Simpson E C, Guatelli S and Haga A 2022 Development of a more accurate Geant4 quantum molecular dynamics model for hadron therapy *Phys. Med. Biol.* **67** 225001
Schiavi A, Senzacqua M, Pioli S, Mairani A, Magro G, Molinelli S, Ciocca M, Battistoni G and Patera V 2017 Fred: a GPU-accelerated fast-Monte Carlo code for rapid treatment plan recalculation in ion beam therapy *Phys. Med. Biol.* **62** 7482–504
Schneider W, Bortfeld T and Schlegel W 2000 Correlation between CT numbers and tissue parameters needed for Monte Carlo simulations of clinical dose distributions *Phys. Med. Biol.* **45** 459–78
Soukup M, Fippel M and Alber M 2005 A pencil beam algorithm for intensity modulated proton therapy derived from Monte Carlo simulations *Phys. Med. Biol.* **50** 5089
Tashima H *et al* 2023 Bench-to-Clinical Transfer of OpenPET: First In-Beam Test in a HIMAC Treatment Room *2023 IEEE Nuclear Science Symp., Medical Imaging Conf. and Int. Symp. on Room-Temperature Semiconductor Detectors (NSS MIC RTSD)* (IEEE) pp 1–1
Tessonnier T, Marcelos T, Mairani A, Brons S and Parodi K 2016 Phase space generation for proton and carbon ion beams for external users' applications at the Heidelberg Ion Therapy Center *Front. Oncol.* **5** 297
Toramatsu C *et al* 2018 Washout effect in rabbit brain: in-beam PET measurements using 10C, 11C and 15O ion beams *Biomed. Phys. Eng. Express* **4** 035001
Toramatsu C *et al* 2022 Measurement of biological washout rates depending on tumor vascular status in 15O in-beam rat-PET *Phys. Med. Biol.* **67** 125006
Toramatsu C, Mohammadi A, Wakizaka H, Nitta N, Ikoma Y, Seki C, Kanno I and Yamaya T 2023 Tumour status prediction by means of carbon-ion beam irradiation: comparison of washout rates between in-beam PET and (dce-mri) in rats *Phys. Med. Biol.* **68** 195005

Vasic V, Parodi K and Pinto M 2024 Evaluating an analytical prediction algorithm of positron emitter distributions in patient data for PET monitoring of carbon ion therapy: a simulation study *Appl. Radiat. Isot.* **213** 111479

Xie Z, Li T, Zhang X, Qi W, Asma E and Qi J 2021 Anatomically aided PET image reconstruction using deep neural networks *Med. Phys.* **48** 5244–58

Yoshida E, Tashima H, Shinaji T, Shimizu K, Wakizaka H, Mohammadi A, Nishikido F and Yamaya T 2017 Development of a whole-body dual ring OpenPET for in-beam PET *IEEE Trans. Radiat. Plasma Med. Sci.* **1** 293–300

Zhang J, Lu Y, Sheng Y, Wang W, Hong Z, Sun Y, Zhou R and Cheng J 2021 A comparative study of two *in vivo* PET verification methods in clinical cases *Front. Oncol.* **11** 617787